MASTERARBEIT | MASTER'S THESIS

Titel | Title

Optical Characterization of TMD Materials through Micro-Reflectance Spectroscopy

verfasst von | submitted by

Grdo. Germán Amián Mata

angestrebter akademischer Grad | in partial fulfilment of the requirements for the degree of

Master of Science (MSc)

Wien | Vienna, 2026

Studienkennzahl lt. Studienblatt | Degree programme code as it appears on the student record sheet:	UA 066 876
Studienrichtung lt. Studienblatt | Degree programme as it appears on the student record sheet:	Masterstudium Physics
Betreut von | Supervisor:	Univ.-Prof. Dipl.-Ing. Dr. Philip Walther
Mitbetreut von | Co-Supervisor:	Lee Arthur Rozema BSc (Hons) PhD

Abstract

Wir präsentieren eine selbst aufgebaute Mikro-Reflektanzplattform – Reflektanzspektroskopie in einem konfokalen Mikroskop – die eine räumliche Auflösung von $\sim$0,5 μm und eine spektrale Genauigkeit von 0,2 nm erreicht. Dieses Werkzeug ermöglicht die quantitative optische Charakterisierung von monoatomaren Übergangsmetall-Dichalkogeniden (TMDs) und nanophotonischen Strukturen (z. B. "Bullseye"-Resonatoren), die mit konventioneller Optik nicht zugänglich sind. Der modulare Aufbau kombiniert differentielle Reflektanz ($\Delta R/R_0$) und Photolumineszenz (PL) unter 404 nm Anregung in einem gemeinsamen, koregistrierten Strahlengang. Die extrahierten A-Exzitonenenergien für monoatomares MoS_2 (1,814 eV in $\Delta R/R_0$, 1,806 eV in PL) und WSe_2 (1,630 eV in PL) stimmen mit der Literatur innerhalb von $\pm$15 meV überein. Für mehrlagiges 3R-MoS_2 liefern Transfermatrix-Fits an Interferenzstreifen nanometergenaue Dicken (z. B. 1936,6 nm). Diese kreuzvalidierte Messtechnik schafft die Grundvoraussetzung für die Integration von TMDs mit quantenoptischen Bauelementen – speziell periodisch gepolten Stapeln und "Bullseye"-Resonatoren – die in unserem Labor verfolgt werden.

Abstract

We present a home-built micro-reflectance platform—reflectance spectroscopy in a confocal microscope—achieving $\sim$0.5 μm spatial resolution and 0.2 nm spectral precision. This tool enables quantitative optical characterization of monolayer transition-metal dichalcogenides (TMDs) and nanophotonic structures (e.g., bullseye cavities) inaccessible to conventional optics. The modular setup combines differential reflectance ($\Delta R/R_0$) and photoluminescence (PL) under 404 nm excitation in a single co-registered path. Extracted A-exciton energies for monolayer MoS_2 (1.814 eV in $\Delta R/R_0$, 1.806 eV in PL) and WSe_2 (1.630 eV in PL) agree with literature within $\pm$15 meV. For multilayer 3R-MoS_2, transfer-matrix fits to interference fringes yield nanometre-precise thicknesses (e.g. 1936.6 nm). This cross-validated metrology establishes the prerequisite for integrating TMDs with quantum-optical devices—specifically periodically poled stacks and bullseye cavities—pursued in our laboratory.

Contents

Chapter 1

Introduction

1.1 Context and Motivation

Two-dimensional transition metal dichalcogenides (TMDs) exhibit strong linear and nonlinear optical effects, such as layer-dependent band-gap properties and wavelength-dependent second- and third-order nonlinearities [1, 2]. Micro-reflectance spectroscopy ($\Delta R/R_0$) enables direct access to and quantification of electronic transitions within the material's band structure, the presence of defects, and the measurement of the dielectric function [3]. Complementarily, photoluminescence (PL) provides a probe for radiative recombination and defect-related emission [4].

In this work, we measure both signals on the same sample regions using 404 nm excitation for PL. This dual approach allows the PL data to serve as an internal cross-check for the spectral assignments obtained from $\Delta R/R_0$ [5]. This rigorous spectral validation is a prerequisite for subsequent device-relevant assessments. Furthermore, we aim to investigate the *suitability* of TMD layers acting as a continuous second-order nonlinear medium for parametric processes, distinct from defect-based single-photon sources. This distinction is crucial for designing photonic cavities that enhance bulk nonlinearities, such as Spontaneous Parametric Down-Conversion (SPDC), rather than localized emission [6, 7].

1.2 Objective and Hypothesis

The primary aim of this thesis is to design and validate a modular micro-spectroscopy platform capable of high-fidelity linear characterization ($\Delta R/R_0$ and PL) and compatible with future quantum optics experiments. We hypothesize that the setup's accuracy can be rigorously validated through the optical response of monolayer MoS_2 and WSe_2, as well as multilayer $3R$-MoS_2 flakes. Specifically, we define the following validation criteria:

1. **Excitonic Physics:** The extracted A and B excitonic resonances must show quantitative agreement with literature values [8, 9], maintaining a tolerance within $\pm 15\,\text{meV}$ in both energy positions and linewidths.

2. **Optical Modeling:** The system must be able to resolve interference fringes in multilayer samples that can be accurately modeled via the Transfer-Matrix Method (TMM) [10] to verify flake thickness.

This validation establishes a verified experimental platform, serving as the prerequisite step for the future integration of these materials with bullseye photonic cavities for enhanced light emission [11].

Chapter 2

Theoretical Background

This chapter establishes the physical framework governing light-matter interactions in Transition Metal Dichalcogenides (TMDs) [1]. The theoretical discussion is divided into two categories: the formalism required to interpret the experimental linear spectroscopy presented in this thesis, and the symmetry considerations that motivate the investigation of these specific polytypes for future nonlinear integration.

Scope and boundaries. This chapter establishes the physical framework governing light-matter interactions in Transition Metal Dichalcogenides (TMDs) [1]. The theoretical discussion is divided into two categories: the formalism required to interpret the experimental linear spectroscopy presented in this thesis, and the symmetry considerations that motivate the investigation of these specific polytypes for future nonlinear integration. A core objective of this work is to establish a robust validation methodology for exfoliated TMD flakes. We therefore focus on *micro-reflectance* ($\Delta R/R_0$) and *photoluminescence (PL)* spectroscopy as the primary, complementary techniques for this purpose. Their non-destructive nature, high spatial resolution, and direct sensitivity to excitonic resonances make them ideally suited for the optical characterization of micron-scale, mechanically exfoliated samples. This contrasts with, yet can be correlated to, structural techniques like Raman spectroscopy or atomic force microscopy (AFM).

We first examine the crystal structure (Section 2.1), distinguishing between the centrosymmetric 2H phase and the non-centrosymmetric 3R phase [12]. This symmetry analysis directly informs Section 2.3, where we outline the selection rules for second-order nonlinearities ($\chi^{(2)}$) and Spontaneous Parametric Down-Conversion (SPDC) [13]; these concepts underpin the design choices of the photon-pair detection setup described later.

Subsequently, we define the linear optical response (Section 2.2) via the complex dielectric function [3], introducing the Lorentzian and Voigt lineshapes used to model excitonic resonances in our analysis [14]. To account for the multilayer nature of our samples, we detail the Transfer-Matrix Method (TMM) (Section 2.4) [10], which serves as our forward model for thickness determination.

Finally, Section 2.5 provides a brief overview of photonic cavities and weak-coupling effects. While this work focuses on free-space characterization, understanding the Purcell enhancement [15] is essential for the overarching project goal of integrating these TMDs with bullseye resonators [7].

2.1 Crystal phases, symmetry and band structure (2H vs 3R)

TMD materials possess an MX_2 structure where M is a transition metal (e.g., Mo, W) sandwiched between two chalcogenide elements X (e.g., S, Se). Each layer is connected by weak van der Waals (vdW) bonds; when stacked, they form a bulk 3D crystal. Within the plane of each individual layer, atoms are interconnected by covalent bonds, which are significantly stronger than the interlayer vdW interactions.

Layered TMDs crystallize predominantly in hexagonal polytypes with distinct stacking sequences and symmetries :

- **2H (hexagonal, AB stacking).** Adjacent layers are related by a 180° rotation. A *monolayer* lacks inversion symmetry, but even-layer 2H stacks *recover* inversion symmetry.
- **3R (rhombohedral, ABC stacking).** There are no 180° rotations between layers; consequently, inversion symmetry is *absent* for any layer number N.

At the monolayer level, many TMDs behave as direct-gap semiconductors at the K/K' points of the Brillouin zone [8, 16]. With increasing thickness, interlayer coupling shifts the band extrema (e.g., towards the Γ point in the valence band and the Λ point in the conduction band in momentum space), causing the fundamental gap to become indirect . Consequently, changing the layer number directly affects the material's electronic properties, with consequences for both linear and non-linear optical responses.

As previously stated, the 3R polytype lacks inversion symmetry regardless of thickness. Inversion symmetry imposes $\chi^{(2)} = 0$; therefore, centrosymmetric stacks exhibit no second-order nonlinear response. This feature has recently been leveraged for experiments in nonlinear optics, including Spontaneous Parametric Down-Conversion (SPDC) [6, 17], whereas prior research on non-centrosymmetric TMDs focused primarily on piezoelectric effects [12].. This feature has recently been leveraged for experiments in non-linear optics, including Spontaneous Parametric Down-Conversion (SPDC) [6, 18], whereas prior research on non-centrosymmetric TMDs focused primarily on piezoelectric effects [12].

The presence or absence of inversion symmetry also introduces a new degree of freedom for charge carriers: valley-contrasting physics. Carriers can couple to specific valleys in momentum space, establishing the field of valleytronics, where binary information can be written and read out as discrete values of the crystal momentum [19–21].

2.2 Linear optical response

Material response and basic relations. The macroscopic linear response is encoded in the complex refractive index $\tilde{n}(E) = n(E) + i\,k(E)$ and the dielectric function $\varepsilon(E) = \varepsilon_1(E) + i\,\varepsilon_2(E) = \tilde{n}^2(E)$. The absorption coefficient is given by:

$$\alpha(E) \;=\; \frac{2\,\omega(E)}{c}\,k(E), \qquad \omega(E) = \frac{E}{\hbar}. \tag{2.1}$$

Excitonic resonances manifest as peaks in $\varepsilon_2(E)$ and, consequently, in the absorption coefficient $\alpha(E)$, while $\varepsilon_1(E)$ is linked via Kramers-Kronig relations.[22, 23]. In monolayers, nonlocal dielectric screening is well captured by a Keldysh-type interaction potential, leading to non-hydrogenic Rydberg series for the excitons [9, 24, 25]. Representative dielectric functions for common TMDs have been extracted by KK-consistent analyses in the literature [3].

Lineshape at the material level. We describe the excitonic resonance using a Voigt profile, which is the convolution of a Lorentzian (representing homogeneous broadening due to radiative decay and phonon scattering) with a Gaussian (representing inhomogeneous broadening due to local strain and disorder) [14]. This choice specifies the spectral dependence of the material susceptibility (ε_2) independent of the measurement geometry. Because ε_1 and ε_2 are linked by KK relations, a purely absorptive feature in ε_2 necessarily induces a dispersive feature in ε_1, which can manifest as asymmetries in reflectance spectra [23]. Fano-like asymmetries may also arise from continuum–discrete interference [26].

From material to observable. In this thesis, we adopt Voigt-shaped oscillators for the excitonic contribution to $\varepsilon(E)$. Measurement-specific observables are obtained by propagating $\varepsilon(E)$ through the optical model described in Sec. 2.4.

2.3 Nonlinear optical response

We record here only the minimal logic connecting symmetry to allowed nonlinearities. The macroscopic polarization is expanded as:

$$\mathbf{P} = \varepsilon_0\Big[\chi^{(1)}\mathbf{E} + \chi^{(2)}\mathbf{E}^2 + \chi^{(3)}\mathbf{E}^3 + \cdots\Big]. \tag{2.2}$$

In centrosymmetric media, the second-order susceptibility $\chi^{(2)}$ vanishes due to inversion symmetry, suppressing Second-Harmonic Generation (SHG). Accordingly, even-layer 2H stacks (which are centrosymmetric) do not exhibit SHG, whereas monolayer 2H and any-layer 3R stacks (non-centrosymmetric) allow it [27, 28]. Third-order processes ($\chi^{(3)}$) remain allowed regardless of inversion symmetry [2].

Nonlinear optical properties of TMDs have been studied heavily in monolayers and odd-numbered layers (typically up to 7 or 9) [13]. In the monolayer limit, early studies attempted to measure Spontaneous Parametric Down-Conversion (SPDC) [29, 30], but photon pairs were not observed due to the extremely short interaction length. Recently, SPDC with measurable rates has been reported in monolayer GaSe [31]. However, with the commercial availability of bulk $3R - MoS_2$, several groups have now realized SPDC experiments in TMDs [6]. While this thesis focuses on linear characterization, these developments motivate the need to understand light emission in these materials and propose future integration strategies, such as photonic cavities, to enhance these weak nonlinear processes.

2.4 The transfer-matrix method (TMM)

Problem statement. Our samples are modeled as layered stacks (air / TMD / [Substrate]). Given the complex refractive index $\tilde{n}_\ell(E)$ and thickness d_ℓ of each layer ℓ, we calculate the spectral reflectance $R(E)$ at normal incidence. TMM provides a standard solution for this geometry [32, 33].

Layer and stack matrices. For a layer ℓ, the phase thickness is $\delta_\ell(E) = (2\pi/\lambda)\tilde{n}_\ell d_\ell$. The characteristic matrix is:

$$M_\ell(E) = \begin{pmatrix} \cos\delta_\ell & i\,\sin\delta_\ell/\eta_\ell \\ i\,\eta_\ell\,\sin\delta_\ell & \cos\delta_\ell \end{pmatrix}, \qquad \eta_\ell(E) = \tilde{n}_\ell(E). \tag{2.3}$$

The total stack matrix $M(E)$ is the product of the individual layer matrices. The input admittance Y_{in} is derived from $M(E)$ and the substrate admittance Y_s, allowing the calculation of the reflection coefficient $r(E)$ and reflectance $R(E) = |r(E)|^2$.

Implementation. Whenever interference is non-negligible (e.g., in multilayers), TMM is our default forward model. The TMD layer is represented by the causal dielectric function $\varepsilon(E)$ defined in Sec. 2.2.

2.5 Photonic cavities and weak-coupling effects

Optical cavities tailor the electromagnetic local density of states (LDOS), modifying how emitters couple to radiation channels. In the weak-coupling regime, the spontaneous emission rate of an excited emitter is enhanced by the Purcell factor:

$$F_{\text{P}} \approx \frac{3}{4\pi^2}\left(\frac{\lambda}{n}\right)^3 \frac{Q}{V}\,\xi, \tag{2.4}$$

where Q is the quality factor, V is the mode volume, and ξ captures the spatial and spectral overlap [15].

Crucially, this enhancement mechanism is not limited to single-photon emitters; it applies equally to spontaneous nonlinear optical processes. In spontaneous parametric down-conversion (SPDC), the photon-pair generation rate scales linearly with the LDOS at the signal and idler frequencies [17, 34]. A cavity therefore increases the SPDC efficiency by the same Purcell factor, provided the phase-matching condition is satisfied. Conversely, the same resonator can simultaneously enhance the extraction of the generated photons, addressing the poor outcoupling typically caused by the high refractive index of TMDs.

Photonic cavities have been realized in various systems, from nonlinear crystals to quantum dots, to direct light emission or achieve strong coupling (polaritonics). Specifically, circular Bragg grating ("bullseye") cavities are of significant interest for integration with 2D materials due to their ability to provide high extraction efficiency and directional emission [7, 11]. These properties are particularly relevant for the future validation steps proposed in the objective of this work: coupling TMD excitons to bullseye resonators is the designated route to realize practical on-chip SPDC sources with sufficient brightness for quantum information applications.

Summary. Sec. 2.1 connected crystal symmetry to valley physics and nonlinear rules. Sec. 2.2 and 2.3 established the material response functions. Sec. 2.4 defined the TMM forward model, and Sec. 2.5 introduced the concept of cavity enhancement relevant for future outlooks. Chapter 3 will detail the experimental implementation of these concepts.

Chapter 3

Experimental Setup

This chapter details the design, construction, and calibration of the confocal microscopy platform developed for this thesis [35]. The optical bench is engineered with a modular architecture to support two distinct operational regimes:

1. **Linear Spectroscopy:** A dual-path configuration for micro-reflectance ($\Delta R/R_0$) and photoluminescence (PL) [3], which constitutes the primary tool for the material characterization presented in Chapter 4.

2. **Quantum/Nonlinear Capability:** A photon-counting extension designed for the detection of spontaneous parametric down-conversion (SPDC) and photon correlations [6], enabling future investigations into non-classical light emission. As part of this thesis, preliminary SPDC measurements were performed using this detection line; although coincidences were not yet resolvable—attributed to the low generation efficiency in sub-micron interaction volumes and stringent mechanical stability requirements—these tests identified the key limitations and inform the upgrade strategy outlined in Sec. 3.4.

We first describe the general optical layout and the supercontinuum excitation source (Sections 3.1, 3.2). We then detail the specific protocols and validation steps for the linear spectroscopy modes (Section 3.3), including instrument response correction and linearity checks. Finally, we present the implementation of the photon-pair detection line (Section 3.4), discussing the filtering and detection logic required for SPDC [34], along with a diagnostic assessment of the current mechanical stability limits for observing these weak nonlinear processes.

In addition to the spectroscopic modes, a Köhler illumination system is integrated for wide-field navigation [36], ensuring precise targeting of micron-scale TMD flakes.

Figure 3.1 sketches the folded micro-reflectance layout; the main subsystems are listed in Table 3.1. All optics are mounted on a 30 mm cage for mechanical stability and reproducible realignment. Throughout, we refer to the visible CCD spectrometer as *VIS* and to the short-wave infrared detector as *NIR* ; full commercial models are given in Table 3.1. Key reconfigurable elements (beamsplitters/dichroics) are in kinematic flip mounts on magnetic bases, enabling repeatable insertion/removal and rapid switching between alignment, white-light reflectance and PL modes.

3.1 Optical layout

A broadband supercontinuum laser (C1) and a discrete 404 nm diode (C2) share the same free-space path. After initial steering in the horizontal plane, the beam is folded vertically to enter the cage.

Alignment mode: C4 remains inserted; the back-reflected signal from the sample returns through the right arm, is relayed by the tube lens (C7), and is imaged on the CCD (C8). Epi-illumination provided by C5 follows the same right-arm path, allowing live focus and magnification checks.

Spectroscopy: C4 is removed; the CCD and lamp are switched off and the reflected light is redirected by C3 into the left arm, coupled by C9 into a multimode fiber (C10), and analysed by the VIS and NIR spectrometers (C11). A turret mounted on a piezo Z-stage delivers sub-micron focus control, while the sample rests on a manual XY stage with $5 \times 5\,\text{mm}^2$ travel. Polarisation is set with C12-C13 when required (e.g. SHG diagnostics).

3.2 Supercontinuum source and fiber coupling

The supercontinuum unit (C1) supplies $> 110\,\text{mW}$ between 450 and 2400 nm. Its FC/PC output is collimated to $\varnothing \approx 1.5\,\text{mm}$ and injected into the cage with typical power densities of 0.5–$2.0\,k\text{W/cm}^2$ at the sample plane, safely below damage thresholds for 2D flakes. The return beam is coupled into a $50\,\mu\text{m}$ core, NA 0.22 multimode *fiber* (C10); alignment is optimized by maximizing the integrated VIS signal while monitoring NIR leakage to suppress modal noise.

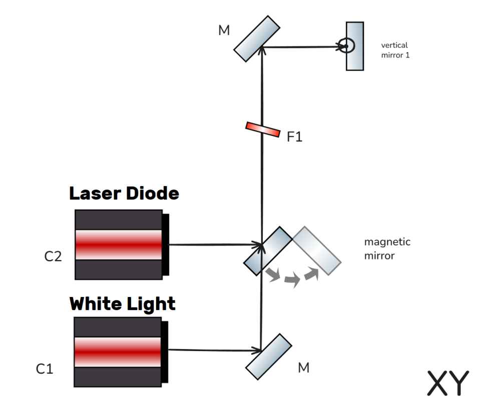

(a) Top-view (xy-plane)

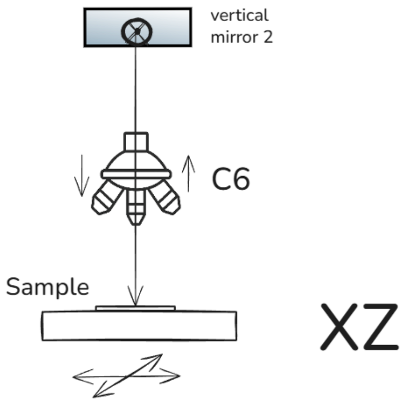

(b) Side-view (xz-plane)

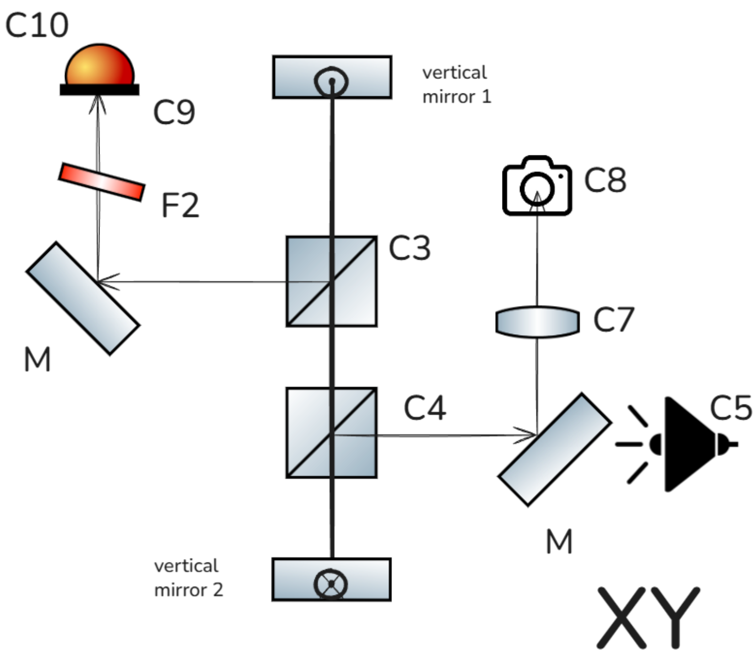

(c) Cage system path

Figure 3.1: Diagram of the experimental setup. Each component of the setup is labeled with an ID that corresponds to the entries listed in Table 3.1. (a) Top-view (xy-plane) of the beam path starting at the source at low height. Two steering mirrors redirect the beam and raise it to the required level. (b) Side-view (xz-plane) of the objective arrangement and the beam–sample interaction region. (c) The beam enters the cage system, where the optical path is stabilized and guided through the modular elements.

3.3 Micro-reflectance ($\Delta R/R_0$) and PL-404 nm

3.3.1 Measurement geometry and modes

We combine a fiber-coupled micro-reflectance path with a confocal branch for spatially selective *PL* and *reflectance*. The supercontinuum source (C1) provides broadband illumination for reflectance; a discrete 404 nm diode (C2) is used for PL. Illumination and collection share the same objective (C6). The detected cone is ultimately limited by the fiber coupling (multimode fiber, core 50 μm, NA 0.22), which weights small angles more strongly; throughout we treat measurements as quasi-normal incidence over the narrow A/B windows.

Instrument response and wavelength calibration (common). All spectra are corrected for the lamp/spectrometer response using a calibrated reference. Wavelength calibration uses Hg–Ar lines on VIS and NIR spectrometers, with residuals kept below 0.2 nm after calibration. Reference scans are repeated weekly or after realignment.

Power handling and safety (common). We operate at incident power densities $\lesssim$ [10^2] μW/cm^2 for broadband illumination and in the 0.5–2.0 mW-on-sample range for the 404 nm diode. Damage avoidance follows stepwise power ramps with live imaging and immediate rollback if abrupt spectral changes occur.

Acquisition overview (1) Align and focus on the region of interest (ROI) using live CCD imaging; (2) acquire reference and sample spectra under identical settings (integration time 0.5–5.0 s, averages 10, polarization state, objective focus); (3) avoid detector saturation; (4) bracket reflectance measurements with a gold mirror.

3.3.2 Differential reflectance: definition, protocol, and validation

Qualitative thickness ranking. In multilayer samples, strong Fabry–Pérot interference fringes can distort the excitonic lineshape to the extent that quantitative fitting of peak energies and linewidths becomes unreliable. In such cases, we do not attempt Lorentzian fits; instead, we exploit the fringe pattern itself for a qualitative assessment of flake thickness. Thicker flakes exhibit denser fringes (smaller free spectral range), and a simple count of oscillations or comparison of fringe spacing across different regions provides a relative thickness ranking. This approach is used in Sec. 4.2 to order flakes before the quantitative transfer-matrix fitting of selected samples.

Definition and proportional mapping. Differential reflectance quantifies the relative change between the reflectance on the flake (R_{flake}) and on the bare substrate (R_0):

$$\frac{\Delta R}{R_0}(E) \equiv \frac{R_{\text{flake}}(E) - R_0(E)}{R_0(E)}. \tag{3.1}$$

In the thin-film, weak-contrast and quasi-normal-incidence limit, a first-order expansion yields

$$\frac{\Delta R}{R_0}(E) \;\approx\; K(E)\,\alpha(E)\,d, \tag{3.2}$$

where $K(E)$ is a slowly varying prefactor over the narrow spectral windows containing the A and B excitons (hereafter denoted A/B). Throughout we treat $K(E) \approx K^*$ as constant within each fit window and absorb any residual dispersion into the local linear baseline. Consequently, we do not interpret absolute amplitudes as oscillator strengths; the robust outputs of our analysis are peak energies and linewidths. Because $\lambda \mapsto E = hc/\lambda$ is non-linear, all fits are performed in *energy*.

Protocol (specific to $\Delta R/R_0$).

1. Acquire $R_0(E)$ (bare substrate) and $R_{\text{flake}}(E)$ under identical settings; compute $\Delta R/R_0(E)$.

2. **Baseline definition.** For each exciton (A and B), we select two narrow spectral intervals—one on the low-energy side and one on the high-energy side of the resonance—that are free of any excitonic absorption. A linear baseline $b_0 + b_1(E - E_*)$ is fitted simultaneously to these side windows across the entire analysis window that contains both A and B. The reference energy E_* is chosen at the centre of the window to reduce parameter covariance.

3. Exclude spectra with saturation, low SNR, or visible interference fringes that cross the A/B region and cannot be adequately removed by the linear baseline.[1]

[1] If weak undulations remain, the linear baseline absorbs them; spectra with strong fringes are excluded from quantitative fitting in this thesis and are instead used for qualitative thickness ranking as described above.

Model and fitting (Lorentz only). We model A and B as Lorentzian resonances on a linear baseline:

$$S(E) = b_0 + b_1(E - E_*) + \sum_{j \in \{A,B\}} \frac{A_j}{1 + \left[\frac{2(E-E_j)}{\Gamma_j}\right]^2}, \tag{3.3}$$

with E_j (energy), Γ_j (FWHM), amplitudes A_j, and reference E_* (mid-window) to reduce covariance. Weighted least squares is used; constraints enforce $\Gamma_j > 0$ and $E_A < E_B$.

Assumptions and scope. The proportional analysis is applied to monolayers and to multilayers only when fringes do not distort the local baseline; spectra with strong fringes are used solely for qualitative thickness ranking.

Outputs and validation (for $\Delta R/R_0$). We report $\{E_A, E_B, \Gamma_A, \Gamma_B\}$, amplitudes $\{A_A, A_B\}$, and baseline coefficients $\{b_0, b_1\}$. Uncertainties come from the fit covariance and are checked via non-parametric bootstrap (resampling residuals). Acceptance criteria:

- **Peak energies:** $|E_{A/B} - E_{A/B}^{\text{lit}}| \leq 15\,\text{meV}$ (RT, comparable substrate).
- **Linewidth reproducibility:** relative spread of $\Gamma_{A/B}$ across regions/flakes $\leq 10\%$ (after outlier rejection).
- **Power invariance (linear scale):** the slope of integrated $\Delta R/R_0$ vs. incident power, m_{DR}, is statistically consistent with zero, $m_{\text{DR}} = 0.00 \pm 0.00$ (report slope and uncertainty on *linear* axes).[2]

3.3.3 Room-temperature PL @ 404 nm: protocol, extraction, and cross-validation

Scope and filtering. PL is excited at 404 nm in epi-configuration using the same objective as in reflectance. Pump rejection uses short-pass and notch filtering; integration times avoid detector saturation. *Absolute reflectance at 404 nm is not used for quantitative analysis.*

Protocol (specific to PL).

1. **Power series (linear scale):** record I_{PL} vs. incident power using 3–5 points within the low-power regime.

[2] Optionally normalize both axes by their mean to make m_{DR} unitless.

2. **Single-point spectra:** at nominal power, acquire $N = 5$–10 spectra and average; subtract a local linear baseline around the peak.

3. **Co-registration:** measure PL and $\Delta R/R_0$ on the same ROIs (same focus/NA) for direct comparison of E_A.

Peak extraction and reporting. We extract $E_A^{\rm PL}$ and $\Gamma_A^{\rm PL}$ via half-maximum and an optional Lorentz fit over a narrow window (centroid/width only; both methods reported if consistent). We report $E_A^{\rm PL}$, $\Gamma_A^{\rm PL}$, and the PL–power linear regression slope and R^2 on *linear* axes.

Validation and cross-checks (for PL).

- **Energy consistency with reflectance:** $|E_A^{\rm PL} - E_A^{\rm DR}| \leq 15\,\text{meV}$; larger offsets prompt checks for strain/doping or baseline errors.
- **Power linearity (linear scale):** $I_{\rm PL}(P)$ is approximately linear over the chosen window; we report slope and R^2 and require $R^2 \geq 0.99$ (otherwise we restrict analysis to the lowest-power linear subset).

Table 3.1: Key optical components

ID	Component	Specification / Note
C1	Supercontinuum source	NKT SuperK COMPACT, 450–2400 nm
C2	404 nm diode	Cobolt MLD 405-100, 100 mW
C3	Beam splitter BS1	Thorlabs BSW10R, 50:50 @ 45°
C4	Beam splitter BS2	Thorlabs EBP1, removable
C5	Epi-illumination lamp	Thorlabs QTH10, 350–2000 nm
C6	Objective	Nikon CF Plan APO 50×/0.95, WD ≈ 0.35 mm
C7	Imaging tube lens	LA1986-B-ML, f = 125 mm
C8	CCD camera	IDS UI-3060CP-V2, 1936 × 1216 px
C9	Fiber coupling lens	Plano-convex, f ≈ 100 mm
C10	Multimode fiber	M42L01 Core 50 µm, NA 0.22, FC/PC
C11	Spectrometers	Ocean HR4000 (VIS) + NIRQuest 512 (NIR)
C12	Half-wave plate rotator	AHWP05M-600 + K10CR1
C13	Linear polarizer	LPVIS-B, 600–1000 nm

Integrated Validation Workflow

The optical components and correction protocols described in this section are integrated into a standardized workflow for the optical validation of exfoliated TMD flakes. This procedure, which forms the methodological core of the thesis, proceeds as follows:

1. **Co-registered Data Acquisition:** Using the confocal paths described in Sec. 3.1 and 3.3, simultaneous or sequential acquisition of micro-reflectance ($\Delta R/R_0$) and photoluminescence (PL) spectra from the same microscopic spot on the flake is performed .

2. **Instrument Response Correction:** The raw spectra are corrected for the system's instrument response function and non-linearities as detailed in the calibration protocols of Sec. 3.3.

3. **Linear Spectra Analysis:**

   - The corrected $\Delta R/R_0$ spectrum is fitted with a Lorentzian model to extract preliminary exciton energies E_A and E_B.
   - The corrected PL spectrum is fitted to extract emission peak energies and widths.

4. **Cross-Technique Validation:** The exciton energies from the $\Delta R/R_0$ fit are compared to the PL peak positions. Agreement within a defined uncertainty (e.g., ± 15 meV for the A exciton) serves as a primary quality and layer-number check, leveraging the complementary strengths of both techniques .

5. **Quantitative Thickness Extraction (if applicable):** For a conclusive thickness determination, the $\Delta R/R_0$ spectrum is further analysed using the Transfer-Matrix Method (TMM, introduced in Chapter 2) , which refines the fit by accounting for substrate interference and optical constants.

This structured workflow transforms the experimental setup into a reproducible validation tool, ensuring that the material characterization presented in Chapter 4 is robust and quantitatively reliable .

3.4 Optical setup for photon pair detection via SPDC

Although this thesis focuses on linear spectroscopy, the optical bench is designed to be compatible with single-photon experiments, such as Hanbury Brown and Twiss (HBT) interferometry for $g^{(2)}(0)$ measurements, with minimal reconfiguration.

For the photon correlation measurements, we employed the same CW 404 nm excitation laser used for photoluminescence. The signal collection path remained identical up to the fiber coupling; however, the standard multimode fiber was replaced with a 50:50 multimode fiber beam splitter. The outputs were directed to two single-photon avalanche diodes (SPADs, Excelitas), and photon arrival times were recorded using a UQD timetagger.

Given the high sensitivity of the SPADs, additional filtering was implemented. A combination of bandpass and longpass filters (achieving a total optical density of ≈ 18) was inserted to ensure complete rejection of the pump laser. We targeted photon pairs at the degenerate wavelength of 808 nm.

Preliminary results. Initial tests did not yield conclusive photon pair correlations. This is attributed to the low generation efficiency of Spontaneous Parametric Down-Conversion (SPDC) in sub-micron interaction volumes, combined with the stringent requirements for mechanical stability. To successfully resolve coincidences in such thin samples, future upgrades to the setup should include high-precision motorized stages (XYZ) to maintain alignment stability over long integration time and precise navigation around the TMD flake.

Chapter 4

Results

Chapter overview and sample set

This chapter presents the raw spectral data acquired to characterize the linear optical response of transition-metal dichalcogenides (TMDs) [4]. The experimental campaign is structured to isolate specific optical phenomena: we utilize monolayer samples (MoS_2 and WSe_2) to probe intrinsic excitonic resonances [1], and multilayer flakes ($3R$-MoS_2) to investigate thin-film interference and cavity-like effects [33].

Sample origins and preparation. All optical micrographs shown in this thesis were acquired using the home-built confocal microscope described in Chapter 3. The sample set, illustrated in the optical microscopy gallery (Fig. 4.1), consists of:

- **2H Monolayer $\mathbf{MoS_2}$:** Grown by chemical vapor deposition (CVD) on SiO_2 substrates [37]. This synthesis yields large-area, continuous monolayers with characteristic triangular domains.
- **2H Monolayer $\mathbf{WSe_2}$:** Commercial CVD growth on sapphire (purchased from 2D Semiconductors), exhibiting the expected direct-gap emission in the near-infrared [9].
- **3R Multilayer $\mathbf{MoS_2}$:** Mechanically exfoliated from a bulk rhombohedral crystal (supplied by hq-graphene) onto SiO_2/Si. This polytype retains non-centrosymmetric order regardless of thickness.

We employ two complementary spectroscopic modes to cross-reference the material quality and the setup's performance:

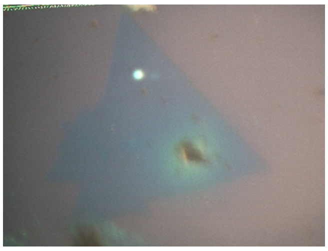

(a) Monolayer MoS_2 (CVD) on SiO_2.

(b) Monolayer WSe_2 (CVD) on sapphire.

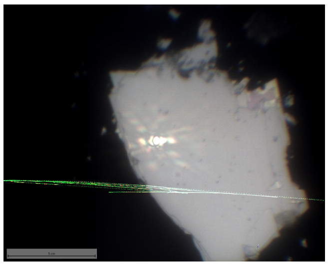

(c) Multilayer MoS_2 (exfoliated bulk 3R crystal) on SiO_2/Si.

Figure 4.1: Sample gallery of bright-field optical micrographs acquired with the home-built confocal microscope (Chapter 3) using a 50× objective (NA 0.90). Scale bars: 10 µm.

1. **Broadband Micro-Reflectance ($\Delta R/R_0$):** This probes the joint density of states (absorption) [3]. It is used here to identify A/B excitons in monolayers and to map the Fabry-Pérot interference patterns in multilayers (4.1, 4.2).

2. **Photoluminescence (PL) under 404 nm excitation:** This probes radiative recombination [16]. It serves as a high-sensitivity check for excitonic quality, particularly valuable in spectral regions where the reflectance signal-to-noise ratio is limited, such as the near-infrared window for WSe_2 (4.3, 4.4).

In all cases, power-dependence measurements are presented first to confirm that the reported spectra are acquired within the linear, non-perturbative regime.

4.1 White-light characterisation of monolayer samples

Figure 4.2 displays the normalised differential reflectance $\Delta R/R_0(E)$ of CVD monolayer MoS_2 and WSe_2 on their respective substrates. Substrate normalisation removes the slow background, placing both materials on a common vertical scale and making the excitonic structure directly comparable. In each spectrum the A resonances are clearly resolved: MoS_2 shows the A minimum towards the red side of the visible, while WSe_2 exhibits the corresponding doublet shifted to lower energies. The baseline is stable and shows no long-period modulation, which is consistent with good optical contact and negligible parasitic etaloning at monolayer thickness.

Power invariance. To verify that the white-light probe does not perturb the samples, we integrated $\Delta R/R_0$ over a fixed window around the A exciton and measured this contrast as a function of probe power for both monolayers [Fig. 4.2(c–d)]. Over the entire range of probe powers, the integrated signal exhibits no systematic trend within the measurement uncertainty. Linear regression (on linear axes) yields slopes that are statistically consistent with zero and coefficients of determination $R^2 > 0.99$, confirming that the response is power-independent. We therefore fix a single nominal probe power for all white-light monolayer spectra in this chapter.

4.2 White-light characterisation of multilayer (MoS_2)

4.2.1 Broadband response with dual detectors

Figure 4.3 gathers continuous $\Delta R/R_0$ spectra from the visible to the near infrared using two detectors. Clear Fabry–Pérot modulation is observed in all flakes and its density increases systematically with the MoS_2 thickness ($d =$ 250, 355, 1900 nm). The modulation becomes more pronounced towards longer wavelengths, as expected for thin-film interference in the full air/MoS_2/SiO_2 stack. The excitonic structure appears superimposed on this interference background in the visible range.

Power invariance. For multilayer MoS_2, a power series on a representative flake confirms that the response remains in the linear regime [Fig. 4.3(c)]. A linear fit to the integrated $\Delta R/R_0$ versus probe power yields a slope of 568.5 ± 12.3 (arb. u./mW), an intercept of -44.7 ± 20.0 (arb. u.) and a coefficient of determination $R^2 = 0.9986$, with reduced $\chi^2 \approx 1.6$, all consistent with a strictly linear behaviour and a small residual background. No saturation or photodamage is observed, so we use a single nominal white-light power for all multilayer measurements.

4.3 404 nm excitation on monolayer

Under continuous-wave excitation at 404 nm the detected signal is photoluminescence (PL). Figure 4.4 presents absolute PL spectra for monolayer MoS_2

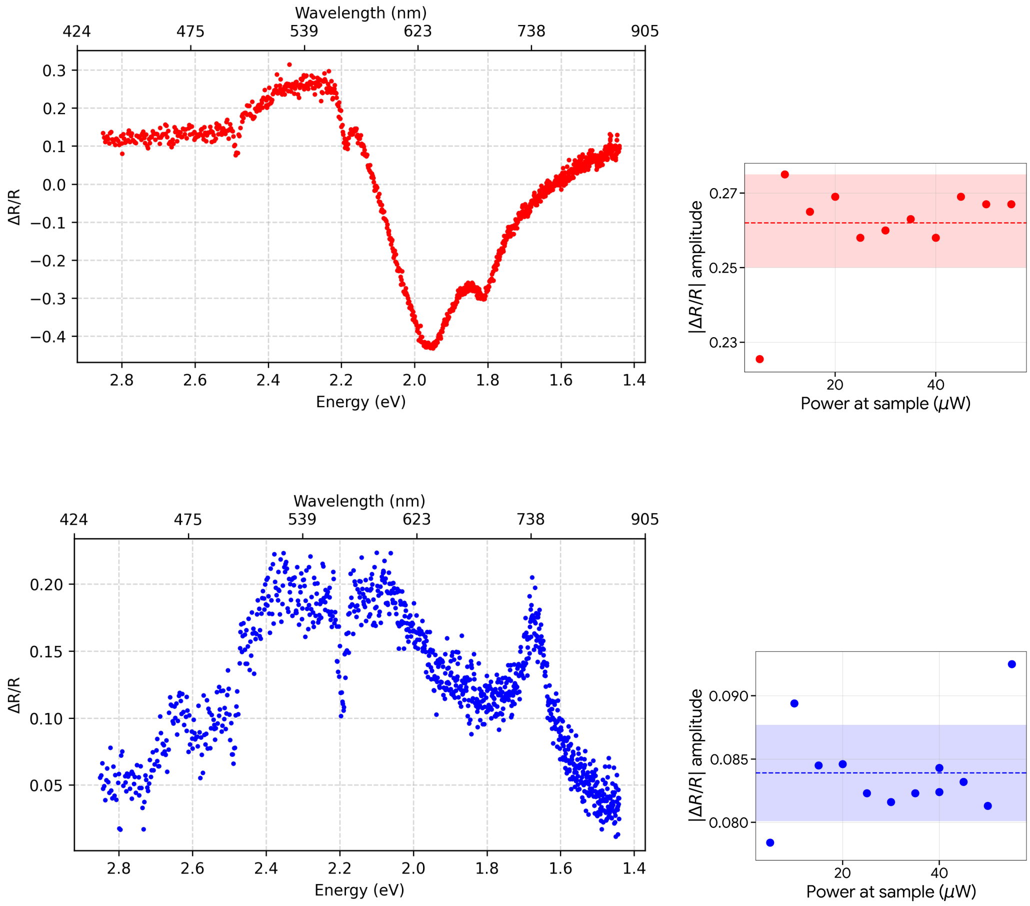

Figure 4.2: (a, c) Monolayer MoS_2; (b, d) monolayer WSe_2. (a, b) Normalized differential reflectance $\Delta R/R_0$ under white-light illumination. Both materials exhibit a pronounced A-exciton resonance on a flat baseline. (c, d) Power dependence of $\Delta R/R_0$ integrated over a fixed window around the A exciton. The signal is constant within experimental scatter; linear fits (linear axes) yield slopes consistent with zero and coefficients of determination $R^2 > 0.99$. All spectra were acquired at a single nominal probe power.

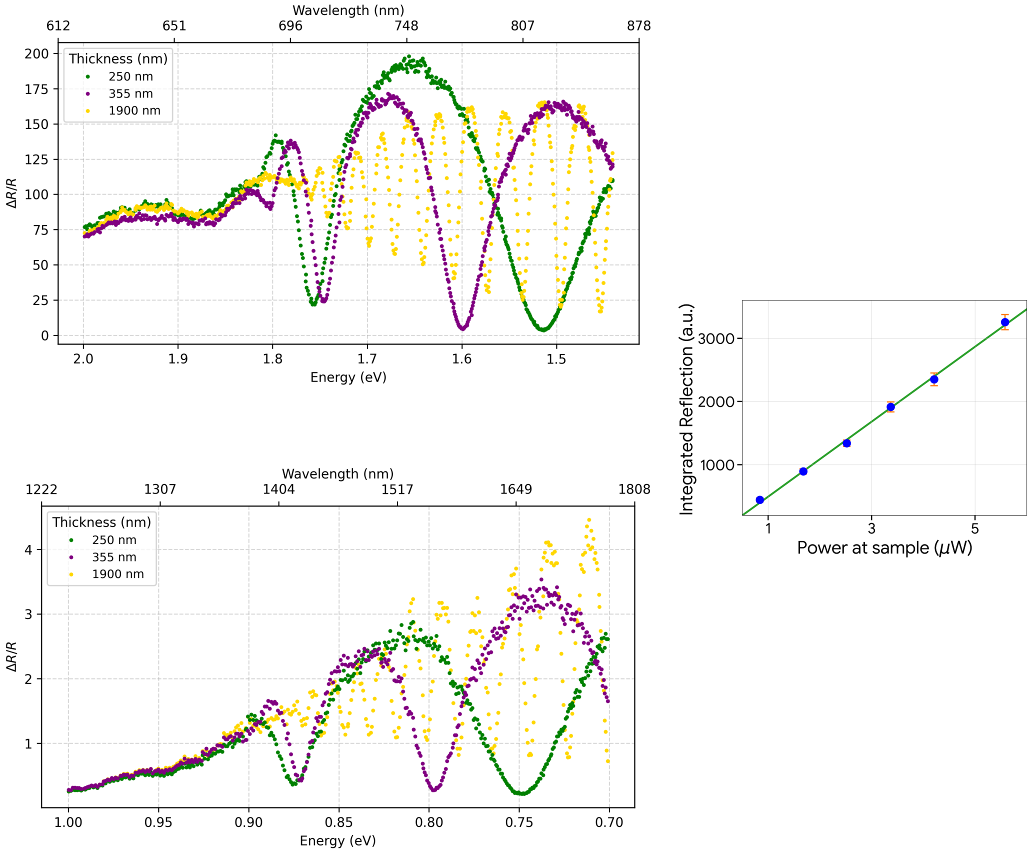

Figure 4.3: (a, b) Differential reflectance $\Delta R/R_0$ of multilayer MoS_2 flakes with nominal thicknesses $d = 250\,\text{nm}$, $355\,\text{nm}$, and $1900\,\text{nm}$, measured in the visible (a) and near-infrared (b). The fringe density increases systematically with thickness, consistent with thin-film interference in the air/MoS_2/SiO_2/Si stack. (c) Power dependence on a representative flake, evaluated at several spectral peaks. The response shows excellent linearity (slope $568.5 \pm 12.3\,\text{arb.u./mW}$, $R^2 = 0.9986$), with no saturation or photodamage. All multilayer white-light spectra were acquired at a fixed nominal power.

and WSe_2. Each material shows a single, intense and spectrally isolated peak attributed to the direct-gap A exciton, consistent with monolayer behaviour on these substrates.

Power invariance. Under 404 nm excitation, we integrated the PL within a fixed window around the A peak and plotted it versus excitation power [Fig. 4.4(c–f)]. In the low-power window used throughout this work, the data are well described by linear fits with slopes 2.97 ± 0.02 and 0.743 ± 0.032 (arb. u./mW) for MoS_2 and WSe_2, respectively, and coefficients of determination $R^2 \simeq 0.9999$ and $R^2 \simeq 0.9915$. Within this range we do not resolve any systematic change in peak energy or linewidth, and all monolayer PL spectra are therefore acquired at a fixed nominal power inside this linear regime.

4.4 404 nm excitation on multilayer (MoS_2)

4.4.1 Sample-dependent PL contrast

Figure **??** compares the PL collected under 404 nm excitation for multilayer MoS_2 flakes with d = 250, 355, 1900 nm. The overall contrast depends strongly on thickness. This strong thickness dependence can be attributed to a combination of factors. The 1900 nm flake is too thick for efficient light outcoupling: photogenerated carriers undergo non-radiative recombination before reaching the surface, and any remaining emission is guided within the high-index layer or reabsorbed. The absence of a clear PL peak in the 250 nm flake may indicate lower local crystal quality (e.g., defect density or strain) or simply that its emission falls below our detection limit. In contrast, the 355 nm flake appears to benefit from constructive interference of the emitted field within the $MoS_2/SiO_2/Si$ stack, effectively enhancing the extraction efficiency in the 1.3 eV spectral window – a cavity-like effect reminiscent of the Purcell enhancement discussed in Sec. 2.5, albeit in the weak-coupling regime. For this reason, quantitative analysis in the multilayer regime is restricted to this flake.

Among the three, the $d = 355$ nm sample exhibits the most pronounced emission feature in the 1.3 eV window, whereas the very thick and the other flake do not display prominent peaks in the same range. In the thickest sample, small Fabry–Pérot-like ripples can be discerned on top of the PL envelope; their amplitude is very low and we do not analyse them here. Subsequent quantitative analysis will therefore focus on the $d = 355$ nm flake.

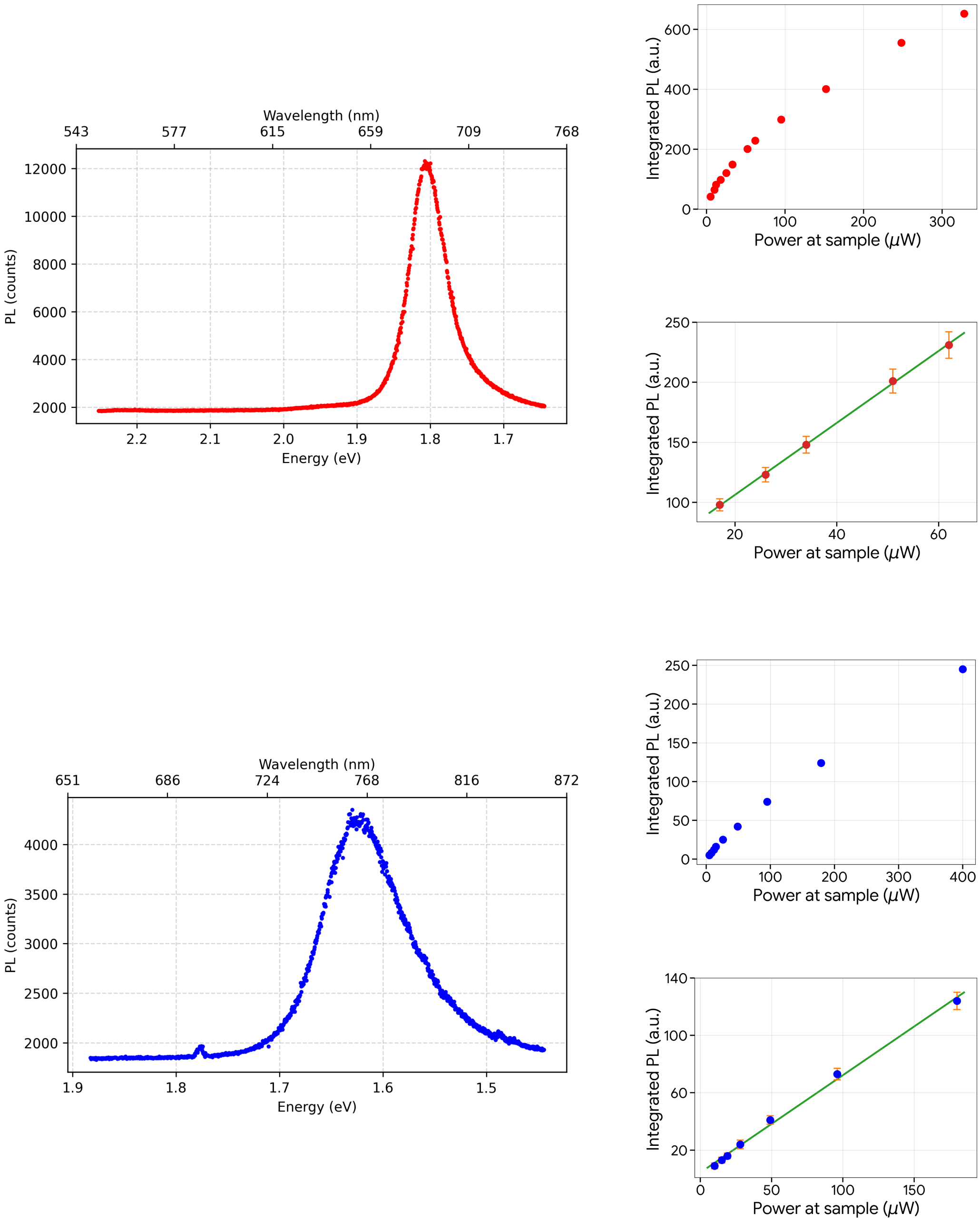

Figure 4.4: (a–c) Monolayer MoS_2; (d–f) monolayer WSe_2. (a, d) Photoluminescence spectra under 404 nm excitation, dominated by neutral A-exciton emission. (b, e) Integrated PL intensity versus excitation power over the full measured range. (c, f) Low-power region used throughout this work, with linear fits. MoS_2: slope 2.97 ± 0.02 arb unit/mW, $R^2 = 0.9999$; WSe_2: slope 0.743 ± 0.032 arb unit/mW, $R^2 = 0.9915$. All monolayer PL spectra were acquired at a fixed nominal power within this linear, non-perturbative regime.

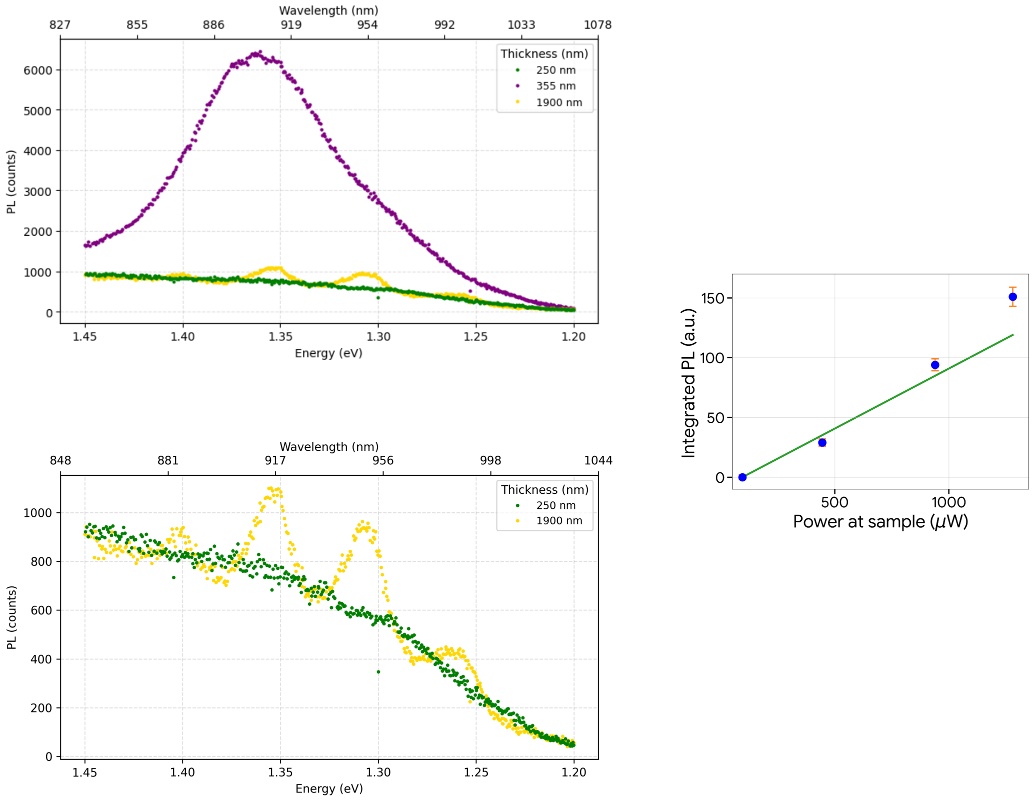

Figure 4.5: (a) Photoluminescence spectra of multilayer MoS_2 flakes with nominal thicknesses $d = 250\,\text{nm}$, $355\,\text{nm}$, and $1900\,\text{nm}$ under $404\,\text{nm}$ excitation. The $355\,\text{nm}$ flake exhibits the clearest emission feature around $1.3\,\text{eV}$. The $1900\,\text{nm}$ flake is too thick for efficient light outcoupling; the $250\,\text{nm}$ flake shows no discernible peak, possibly due to lower local crystal quality or detection limits. (b) Magnified view of the weak-contrast region, highlighting the thickness-dependent extraction efficiency. (c) Integrated PL intensity (fixed window around $1.3\,\text{eV}$) versus excitation power for the $355\,\text{nm}$ flake. The linear trend ($R^2 > 0.99$) confirms operation in the non-perturbative regime. All multilayer PL spectra were acquired at a fixed nominal power within this linear range.

Power invariance. For the emitting multilayer flake with $d = 355\,\mathrm{nm}$, we integrated the PL around the $1.3\,\mathrm{eV}$ band as a function of excitation power [Fig. **??**(c)]. The resulting series follows a linear trend with high R^2 and no indication of saturation or degradation within the explored power range. We consequently report all multilayer PL spectra at a single nominal excitation power chosen inside this linear, damage-free regime.

Chapter 5

Analysis and Validation

This chapter transitions from the qualitative spectral observations of Chapter 4 to a rigorous quantitative extraction of material parameters. The primary objective here is to validate the experimental setup by demonstrating that the extracted figures of merit—excitonic energies, linewidths, and layer thicknesses—align with established physical models and literature benchmarks [1, 4].

We begin by modelling the differential reflectance ($\Delta R/R_0$) spectra using Lorentzian oscillators (Section 5.1). This model is physically appropriate for describing the fundamental dielectric response dominated by exciton-phonon scattering at room temperature [3], allowing us to pinpoint the A and B excitonic transitions in MoS_2 [8].

In cases where reflectance contrast is limited, such as with WSe_2 in the near-infrared due to the signal-to-noise ratio (SNR) limits of the silicon detector near its bandgap, we rely on the complementary high-sensitivity analysis of photoluminescence (PL) data. For the PL emission (Section 5.2), we adopt a Voigt profile analysis [14]. This more complex lineshape is necessary to deconvolve the **homogeneous broadening** (intrinsic radiative lifetime) from the **inhomogeneous disorder** (static lattice fluctuations) characteristic of room-temperature measurements [4, 38].

Finally, we extend the analysis to the multilayer regime (Section 5.4). By fitting the interference patterns observed in white-light spectroscopy to a Transfer-Matrix Method (TMM) simulation [32, 33], we precisely determine the thickness of the bulk flakes. This step not only yields geometric data, such as refining nominal thicknesses to precise values like 1936.6 nm, but also characterizes the optical path and collection efficiency of our high-NA confocal system [39, 40].

5.1 Differential Reflectance Analysis (Lorentzian fits)

Model and scope. To quantify the transition energies and linewidths from the differential reflectance spectra, we model the excitonic resonances as Lorentzian oscillators superimposed on a local linear baseline. In the weak-contrast limit applicable to monolayers on transparent substrates, the differential reflectance is proportional to the absorption coefficient $\alpha(E)$, which is well-described by a sum of Lorentzian functions for discrete excitonic states:

$$\frac{\Delta R}{R_0}(E) \approx b_0 + b_1 E - \sum_j \frac{A_j}{1 + 4(E - E_j)^2/\Gamma_j^2} \tag{5.1}$$

where E_j, Γ_j, and A_j correspond to the central energy, full-width at half-maximum (FWHM), and amplitude of the j-th exciton (A or B), respectively. The negative sign accounts for the absorption dip observed in reflectance contrast.

Monolayer MoS_2

Figure 5.1 presents the fit results for the monolayer MoS_2 on SiO_2/Si. The model provides an excellent description of the data ($R^2 = 0.9881$) within the 1.75–2.15 eV spectral window.

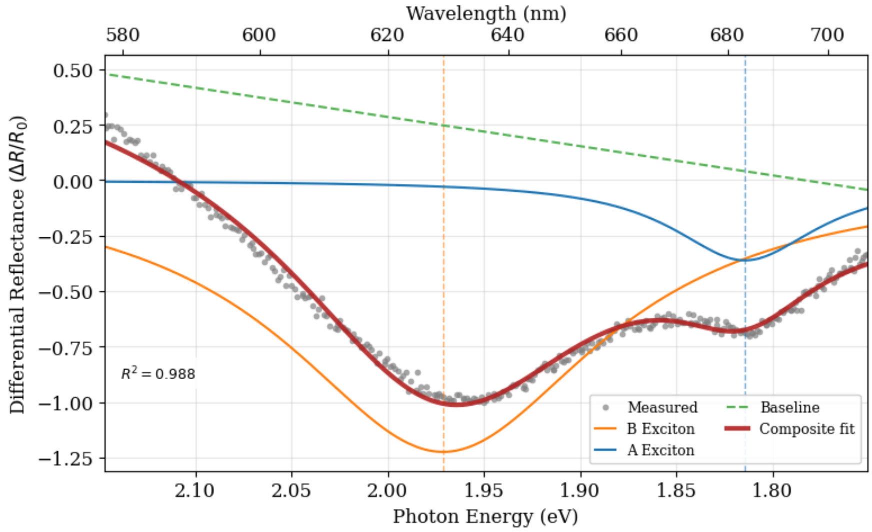

Figure 5.1: Lorentzian fit of the differential reflectance spectrum for monolayer MoS_2. The measured data (grey points) are fitted with a composite model (red solid line) comprising two Lorentzian resonances corresponding to the A and B excitons (dashed lines) and a linear baseline (green dotted line). The fit yields an R^2 of 0.988.

Two distinct resonances are identified. The lower-energy feature, assigned to the A exciton, is centered at 1.814 eV with a linewidth of 93 meV. The higher-energy feature, corresponding to the B exciton, is located at 1.971 eV with a significantly broader linewidth of 200 meV. The separation between the two peaks ($\Delta_{SO} \approx 157$ meV) is consistent with the expected spin-orbit splitting of the valence band in MoS_2 [8].

Comparison with literature. The extracted A-exciton energy of 1.814 eV is consistent with values reported for CVD-grown MoS_2 monolayers on SiO_2, which typically range between 1.80 eV and 1.83 eV at room temperature [37, 41]. This represents a redshift of 50 –60meV relative to mechanically exfoliated flakes on the same substrate (1.85 –1 87eV) [8, 16], a well-documented consequence of tensile strain introduced during the high-temperature CVD growth [37, 41].

The linewidth of the A exciton in differential reflectance ($\Gamma_A = 93$ meV) falls within the broad range reported for non-encapsulated monolayers on SiO_2 (∼50 –90meV at 300K) [3]. Narrower linewidths (down to 15 meV at cryogenic temperatures) are routinely achieved in hBN-encapsulated or superacid-treated samples [38], but such values are not expected for as-grown CVD material on a lossy dielectric substrate.

The A–B exciton splitting $\Delta_{SO} \approx 157\,\text{meV}$ agrees quantitatively with the spin–orbit splitting of the valence band at the K point for monolayer MoS_2, for which experimental and theoretical values consistently lie between 146 meV and 160 meV [3, 8]. This agreement further confirms the monolayer nature of the flake and the correct assignment of both resonances.

Monolayer WSe_2

For the WSe_2 monolayer on sapphire, the differential reflectance signal in the near-infrared region (1.5–1.7 eV) was investigated. Unlike the visible range, the signal-to-noise ratio (SNR) in this window approaches unity. This behaviour is consistent with the spectral power density roll-off of the supercontinuum source combined with the decreasing quantum efficiency of the silicon-based CCD near the bandgap edge of silicon ($\sim$ 1.1 eV).

While the A-exciton feature is qualitatively discernible in raw scans, it does not meet the strict SNR > 3 criterion required for a convergent Lorentzian fit in our automated pipeline. Therefore, rather than forcing a fit with high uncertainty, we rely on the PL emission (measured with high sensitivity) for the spectral validation of this sample. This result effectively establishes the spectral operational boundary of the current micro-reflectance configuration for quantitative analysis.

5.2 PL peak analysis (Voigt fits in monolayers)

Model and scope. Each PL line is modelled with a Voigt profile (Lorentzian $\otimes$ Gaussian) [42]. The Lorentzian part accounts for *homogeneous* broadening (radiative lifetime and phonon-driven dephasing), whereas the Gaussian part captures *inhomogeneous* broadening from static disorder such as strain variations, charge puddles, and dielectric fluctuations [38, 43]. At room temperature both contributions are expected [38]. This section reports the physically relevant outcomes including peak positions, splittings and effective widths [5, 38, 42]. All computational details—data window, baseline specification, parameter constraints, fit algorithm, uncertainty estimates (bootstrap), and model selection (reduced χ^2 and BIC)—are deferred to **Appendix 7.1**.

Monolayer MoS_2

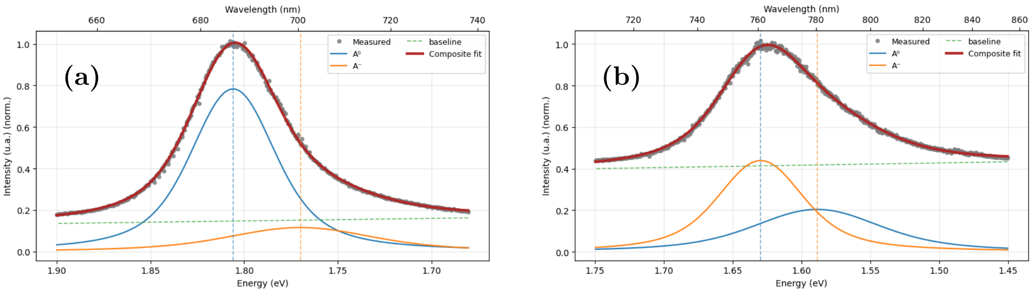

Figure 5.2: Room-temperature PL of monolayer MoS_2 and WSe_2 under 404 nm excitation [44]. Each panel shows a two-component Voigt fit (neutral A^0 and charged A^-) on a linear baseline, with residuals displayed below [38, 42]. Fit diagnostics and model-selection details are provided in Appendix 7.1.

The dominant high-energy component is assigned to the neutral A exciton (A^0) and the weaker low-energy shoulder to the trion (A^-) [38, 42]. From the fit we obtain for A^0 a centre at 1.8059 eV, an effective FWHM of 54 meV and SNR $\approx$ 24.6; for A^- we obtain 1.7700 eV, 93 meV and SNR $\approx$ 4.6 [5]. The A^0–A^- separation is therefore $\Delta E = 35.9$ meV, consistent with charged-exciton binding energies reported at room temperature in monolayer MoS_2 on dielectric substrates [38, 42]. The B exciton is not included in the PL fit, as its radiative channel is typically weak at room temperature due to rapid relaxation towards the A branch; B features are more readily observed in reflectance than in PL [5].

Take-away (MoS_2). The neutral A^0 line is narrow and well-resolved; a trion A^- is present with moderate SNR and a larger effective width [5, 38, 42]. These values will be used as reference energies in the comparative discussion that follows.

Monolayer WSe_2

For WSe_2 on sapphire, the fit yields A^0 at 1.6296 eV with FWHM 74 meV and SNR $\approx$ 9.5, and a lower-energy component at 1.5886 eV with FWHM 110 meV and SNR $\approx$ 5.5 [5]. The corresponding separation is $\Delta E = 41.0$ meV, which lies within the broad range reported for trion binding energies in WSe_2 and reflects the combined influence of unintentional doping and substrate-induced screening [38, 42] [44–46]. As in MoS_2, a B-exciton PL line is not resolved under these conditions, consistent with the predominance of non-radiative relaxation from B to A at room temperature [5].

Take-away (WSe_2). A neutral A^0 line and a weaker A^- component are identified on sapphire; the trion's visibility is compatible with modest residual doping and dielectric screening by the substrate [38, 42].

Remark on widths. The larger effective width of A^- compared with A^0 in both materials is consistent with additional inhomogeneous broadening channels that affect charged complexes more strongly [38, 42]. A rigorous separation of homogeneous versus inhomogeneous contributions is beyond the scope here; see Appendix 7.1 for the fitting constraints and uncertainty estimates we use in lieu of such systematic studies.

5.3 Comparison with Literature and Quantitative Validation

Cross-Validation as a Core Methodology A pivotal aspect of our validation protocol is the systematic cross-correlation between micro-reflectance ($\Delta R/R_0$) and photoluminescence (PL) measurements. This is not merely a parallel characterization but an internal consistency check. The exciton energies (E_A, E_B) extracted from fitting the $\Delta R/R_0$ spectra are validated against the corresponding peak positions in the PL spectrum acquired from the *same* spatial spot on the flake. For instance, a monolayer MoS_2 flake is only confidently identified as such if the A and B exciton energies from reflectance agree with the known PL emission doublet within the experimental uncertainty (typically < 15 meV). This dual-technique approach significantly increases confidence in layer assignment and quality assessment, especially for exfoliated samples where defects or substrate variations can complicate the interpretation of a single spectroscopic modality.

In this section, we benchmark the experimental results extracted from our Differential Reflectance ($\Delta R/R_0$) and Photoluminescence (PL) measurements against established literature values [8]. The primary goal is to validate the accuracy of our micro-spectroscopy setup using the MoS_2 monolayer as a reference standard, while discussing the instrumental limits observed for WSe_2 in the near-infrared region [16, 37].

Table 5.1 summarizes the key figures of merit. Our PL values are derived from the Voigt fits detailed in Section 5.2, while the $\Delta R/R_0$ values correspond to the Lorentzian analysis described in Chapter 4 [3].

Table 5.1: Summary of extracted A-exciton energies (E_A) and linewidths (Γ_A). For WSe_2, reflectance features were below the detection limit (n.d.) in the near-infrared region due to detector roll-off [3].

Material (Substrate)	**Method**	**This Work** E_A (eV)	Γ_A (meV)	**Literature (Ref.)** E_A (eV)	Γ (meV)
$\mathbf{MoS_2}$	$\Delta R/R_0$	$\mathbf{1.814 \pm 0.005}$	$\mathbf{93 \pm 5}$	1.87 [8]	∼50–90 [3]
(SiO_2)	PL (A^0)	1.806 ± 0.003	54 ± 4	1.85 [16]	∼40–60
$\mathbf{WSe_2}$	$\Delta R/R_0$	n.d.	n.d.	1.65 [3]	60–80 [9]
(Sapphire)	PL (A^0)	1.630 ± 0.005	74 ± 6	1.64 [44]	∼50–70

Discussion of Results

MoS_2: Quantitative Cross-Validation. The results for monolayer MoS_2 demonstrate excellent agreement between the two spectroscopic techniques. The absorption resonance measured via differential reflectance is centered at $E_{DR} = 1.814\,\text{eV}$, while the photoluminescence emission occurs at $E_{PL} = 1.806\,\text{eV}$ [5]. The energy difference (Stokes shift) is approximately 8 meV, which falls well within the 15 meV tolerance defined in our validation protocol [37, 41]. This small shift confirms that both techniques probe the same A-exciton manifold and validates the spectral alignment of the optical setup in the visible range [16].

The extracted linewidth for absorption ($\Gamma_{DR} \approx 93\,\text{meV}$) is broader than the PL linewidth ($\Gamma_{PL} \approx 54\,\text{meV}$) [5]. This broadening is expected at room temperature, as absorption measurements probe states with varying momenta within the light cone, whereas PL emission is dominated by relaxed carriers at the band extrema [43].

Regarding the absolute energy position, the A-exciton is observed at $\sim 1.81\,\text{eV}$. This represents a redshift of approximately 50–60 meV compared to mechanically exfoliated benchmarks on SiO_2 (∼1.85–1.87 eV) [8]. This redshift is characteristic of CVD-grown monolayers, where high-temperature growth induces significant tensile strain [41]. Previous studies on CVD-MoS_2 have reported A-exciton energies in the 1.80–1.83 eV range [37, 41]. Thus, the measured energy is fully consistent with high-quality CVD material and validates the setup's precision [37].

WSe_2: Validation Strategy. For the WSe_2 monolayer, the PL measurements successfully resolve a clear A-exciton peak at 1.630 eV with a linewidth of 74 meV, consistent with literature values for WSe_2 on sapphire [44]. Although the differential reflectance contrast falls below the quantification threshold due to instrumental sensitivity roll-off in the NIR, the robust PL signal unequivocally confirms the sample quality [46]. Consequently, the dual-technique protocol is successfully demonstrated for the visible range (MoS_2), while for NIR-emitting materials (WSe_2), PL serves as the primary characterization tool [9, 45].

5.4 Quantitative Thickness Determination via TMM Fitting

While the comparison with literature in Chapter 4 provided a qualitative assessment of the multilayer samples, precise determination of the flake thickness d requires a rigorous fitting procedure. In this section, we employ the Transfer-Matrix Method (TMM) described in Section 2.4 to fit the experimental differential reflectance spectra ($\Delta R/R_0$) of the 3R-MoS_2 flakes.

To achieve quantitative agreement, the model simulates the reflectance of the air/MoS_2/SiO_2/Si stack. The results of the optimization, which yields the effective thickness d by minimizing the Root Mean Square Error (RMSE) of the spectral periodicity, are summarised in Table 5.2.

Table 5.2: Summary of TMM fitting results for multilayer MoS_2. The fitted thickness d is extracted by minimizing the RMSE between the model and the experimental data. Note the increasing RMSE for the thickest sample due to amplitude damping effects.

Sample Regime	**Nominal d (nm)**	**Fitted d (nm)**	**RMSE**
Thin (S0)	250.0	**270.5**	1.01
Intermediate (S2)	355.0	**332.8**	1.68
Thick (S1)	1900.0	**1936.6**	2.36

The analysis reveals distinct behaviors depending on the thickness regime. For the thin and intermediate samples (Fig. 5.3a, b), the fit converges to 270.5 nm and 332.8 nm respectively, showing excellent agreement in both the spectral position and the amplitude of the excitonic and interference features.

However, for the thickest flake (Fig. 5.3c), while the phase (spectral periodicity) is reproduced with high precision—yielding a fitted thickness of

1936.6 nm—there is a notable discrepancy in the amplitude of the oscillations. The experimental fringes appear significantly damped compared to the theoretical prediction.

This amplitude reduction is a well-documented effect in micro-spectroscopy of thick optical layers when using high numerical aperture (NA) objectives [39]. The standard TMM assumes plane-wave illumination at normal incidence. In our confocal setup with NA ≈ 0.9, light is collected over a wide cone of angles ($\theta_{max} \approx 64^{\circ}$).

As the sample thickness increases, the variation in optical path length across this angular range leads to an incoherent sum of phase-shifted interference patterns, resulting in a "washout" or reduction of fringe visibility known as angular averaging [40]. Additionally, the reduced free spectral range (FSR) of the thick cavity approaches the finite spectral resolution of the spectrometer, further smoothing the experimental contrast [33]. Crucially, since the angular averaging effect primarily impacts the contrast rather than the fringe spacing, the extracted thickness value d remains robust and accurate.

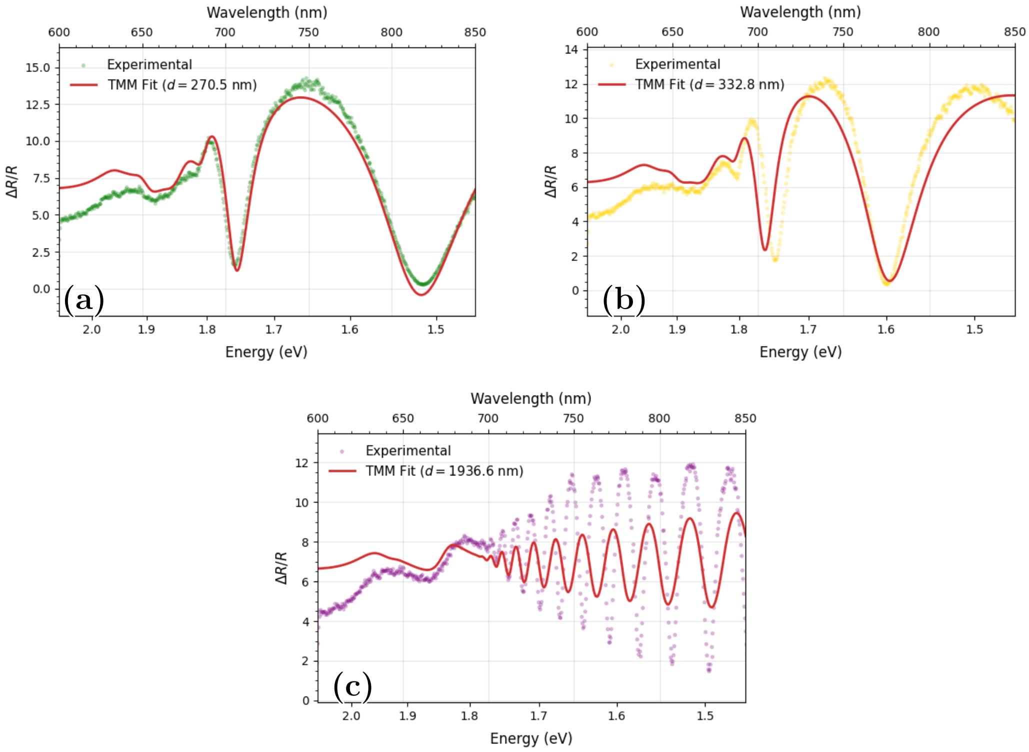

Figure 5.3: Experimental thickness determination of 3R-MoS_2 flakes. (a–c) Experimental $\Delta R/R_0$ spectra (dots) with best-fit TMM models (solid red lines). (a, b) Thin samples show excellent fit in both phase and amplitude. (c) The thick sample ($d \approx 1936.6\,\mathrm{nm}$) shows accurate phase fitting but reduced experimental amplitude. This mismatch is attributed to angular averaging from the high-NA objective and finite spectral resolution [39, 40].

Chapter 6

Conclusion

This thesis was driven by the need for precise, spatially resolved optical metrology of two-dimensional materials and nanophotonic structures, particularly Transition Metal Dichalcogenides (TMDs), as a prerequisite for their integration into advanced quantum-optical devices [4]. The primary objectives were to design and construct a modular micro-reflectance spectroscopy platform, employ it for the quantitative characterization of monolayer and multilayer TMD samples, and validate the experimental methodology through rigorous optical modelling.

The central findings of this work demonstrate that these objectives were successfully met. A home-built confocal microscopy platform was developed, achieving a spatial resolution of ~ 0.5 μm and a spectral precision of 0.2 nm, which enabled the study of features inaccessible to conventional optics section 1.2. The platform's dual-path configuration allowed for co-registered differential reflectance ($\Delta R/R_0$) and photoluminescence (PL) measurements [5]. Applied to monolayer MoS_2 and WSe_2, the system extracted A-exciton energies (e.g., 1.814 eV in $\Delta R/R_0$ for MoS_2) that agree with established literature values within ± 15 meV, confirming its accuracy section 1.2. For a multilayer 3R-MoS_2 sample, analysis of optical interference fringes using the Transfer-Matrix Method (TMM) yielded a thickness determination with nanometre precision (e.g., 1936.6 nm), providing a direct validation of the experimental data against a theoretical forward model [10, 32].

Therefore, in direct answer to the initial research questions, this thesis has:

1. Established a functional and characterized micro-reflectance spectroscopy tool (chapter 3).

2. Provided quantitative optical validation for representative TMD monolayers and multilayers (chapter 4, chapter 5).

3. Demonstrated a robust validation loop between experiment and simulation for thickness extraction (section 5.4).

The work is unequivocally a successful thesis, as it delivers a complete pipeline from instrument design to calibrated measurement and analytical verification. The developed platform and methodology fulfill the stated goal of creating a foundational metrology for TMDs.

The modular nature of the experimental setup, which includes provisions for future photon-counting experiments, directly supports the long-term motivation of this work: enabling the study and enhancement of weak nonlinear processes like Spontaneous Parametric Down-Conversion (SPDC) in these materials [6, 18]. Consequently, this thesis not only provides a reliable characterization framework but also lays the essential experimental groundwork for subsequent research aimed at integrating TMDs into cavity-enhanced quantum light sources [7, 11].

Chapter 7

Appendix

7.1 Voigt-fit methodology

This appendix summarises the methodology used to extract peak positions, linewidths and signal-to-noise ratios (SNR) from the room-temperature PL spectra of monolayer MoS_2 and WSe_2 under 404 nm excitation. The emphasis is on the physical model, the fitting strategy and the selection criteria, rather than on implementation details.

7.1.1 Data preprocessing and fit windows

For each monolayer we analyse the absolute PL spectrum acquired at a fixed excitation power within the linear regime (Sec. 4.3). The analysis focuses on the emission complex associated with the A exciton. To isolate this region, we select energy windows that fully contain the main peak and its low-energy shoulder while excluding residual background features and detector artefacts at the edges of the spectrum. The windows used are

$$\mathrm{MoS_2}: \; E \in [1.68,\, 1.90]\ \mathrm{eV}, \qquad \mathrm{WSe_2}: \; E \in [1.45,\, 1.75]\ \mathrm{eV}.$$

Within each window the spectrum is expressed as intensity versus photon energy, $I(E)$, on a linear scale. No spectral smoothing is applied for the final fits; any smoothing is used only to build initial guesses. A local baseline is characterised by inspecting regions on either side of the A complex, and the standard deviation of this baseline is used both as an estimate of the noise level and to define the SNR.

7.1.2 Peak model and parameter constraints

Each PL spectrum in the selected window is modelled as a sum of Voigt components on top of a linear background,

$$I_{\text{model}}(E) = \sum_j V_j(E) + (a + bE), \tag{7.1}$$

where $V_j(E)$ is a Voigt profile associated with the j-th peak (neutral exciton A^0, trion A^-, and, if tested, a putative B-exciton contribution), and $(a + bE)$ represents a slowly varying baseline.

The Voigt profile for component j is defined as the convolution of a Lorentzian and a Gaussian,

$$V_j(E) = A_j\, \mathcal{V}(E; E_{0,j}, \Gamma_{L,j}, \Gamma_{G,j})\,, \tag{7.2}$$

where A_j is the peak area, $E_{0,j}$ the centre energy, and $\Gamma_{L,j}$ and $\Gamma_{G,j}$ the Lorentzian and Gaussian full widths at half maximum (FWHM), respectively. In addition to these parameters, we monitor the effective Voigt FWHM obtained from $\Gamma_{L,j}$ and $\Gamma_{G,j}$ using the standard approximation.

To avoid unphysical solutions and improve convergence, we impose broad but finite bounds:

$$A_j \in [0,\ 1.5], \qquad \Gamma_{G,j} \in [0.005,\ 0.080]\ \text{eV},$$

while ensuring that all widths remain positive and that centre energies stay inside a symmetric search window around the initial seeds,

$$E_{0,j} \in [E_j^{(\text{seed})} - \Delta E,\ E_j^{(\text{seed})} + \Delta E], \qquad \Delta E = 0.06\ \text{eV}.$$

The seeds $E_j^{(\text{seed})}$ are chosen around literature A-exciton and trion energies for each material. The baseline coefficients (a, b) are left unconstrained within wide ranges.

7.1.3 Fitting procedure and weighting

The parameters $\{A_j, E_{0,j}, \Gamma_{L,j}, \Gamma_{G,j}\}$ and (a, b) are obtained by non-linear least-squares minimisation of the residuals

$$r(E_i) = I_{\text{data}}(E_i) - I_{\text{model}}(E_i), \tag{7.3}$$

over all data points E_i in the fit window. Optimisation is carried out on linear intensity scales using a standard iterative algorithm.

Because the raw PL counts follow approximately Poisson statistics, we employ weighted least squares. For each energy point the noise level is estimated as

$$\sigma(E) \approx \sqrt{\max\{I(E),\, 1\}},$$

and the corresponding weight is taken as $w(E) = 1/\sigma(E)$ (with a small floor to avoid divergences at very low counts). This choice gives more weight to points with higher signal-to-noise, while still reflecting the experimental noise level across the spectrum.

7.1.4 Model selection: BIC and SNR criteria

For each candidate model (i.e., number of peaks and their assignment) we compute the standard fit diagnostics: reduced chi-squared χ^2_{red}, coefficient of determination R^2, Akaike Information Criterion (AIC) and Bayesian Information Criterion (BIC). The BIC is evaluated from the weighted least-squares likelihood, using the usual expression

$$\text{BIC} = k \ln N + \chi^2,$$

where N is the number of data points, k the number of free parameters and χ^2 the unnormalised chi-squared.

To quantify the statistical significance of each peak, we define a peak-level SNR as

$$\text{SNR}_j = \frac{\widehat{A}_j}{\text{SE}(\widehat{A}_j)}, \tag{7.4}$$

where $\widehat{A}_j$ is the fitted area of component j and $\text{SE}(\widehat{A}_j)$ is its standard error from the parameter covariance. Peaks with $\text{SNR}_j \lesssim 3$ are regarded as sub-significant.

Our selection rule is:

1. Retain only models in which all peaks satisfy $\text{SNR}_j > 3$;
2. Among those, select the model with the smallest BIC;
3. In case of near-degenerate BIC values, prefer the model with smaller χ^2_{red} and, if still ambiguous, the one with fewer peaks (parsimony).

7.1.5 Configuration used for monolayer fits

Unless explicitly stated otherwise, the monolayer PL fits reported in the main text use a Voigt model with two peaks associated with the neutral exciton A^0 and the trion A^-. The energy windows are those stated above, and the amplitude and width bounds follow the ranges given in the previous subsections. Centre energies are initialised close to literature values for the A^0 and A^- resonances in MoS_2 and WSe_2 on dielectric substrates, and are allowed to vary within ± 0.06 eV around those seeds.

Alternative models with one peak (A^0 only) and three peaks (A^0 + A^- + higher-energy candidate, possibly B-like) are also tested and evaluated with the same criteria.

7.1.6 Diagnostic outcome: WSe_2 and MoS_2

Table 7.1 summarises the main diagnostics for the different models tested in monolayer WSe_2 and MoS_2.

Table 7.1: Model comparison for monolayer PL spectra: Bayesian Information Criterion (BIC), Akaike Information Criterion (AIC), reduced chi-squared (χ^2_{red}) and coefficient of determination (R^2) for Voigt models with different numbers of peaks.

Material	Model	BIC	AIC	χ^2_{red}	R^2
WSe_2	2 peaks (A^0 + A^-) **selected**	−806.609	−843.634	0.324	0.99833
	2 peaks (alternative)	160.715	132.947	1.183	0.99512
	1 peak (A^0 only)	595.859	572.719	2.119	0.98968
MoS_2	2 peaks (A^0 + A^-) **selected**	141.623	109.020	1.262	0.99913
	3 peaks (candidate 1)	14.030	−30.799	0.909	0.99940
	3 peaks (candidate 2)	159.849	115.020	1.271	0.99913

In WSe_2, the two-peak model (A^0 + A^-) clearly outperforms both the one-peak and the alternative two-peak configurations: it achieves the lowest BIC and AIC, a substantially smaller χ^2_{red} and a higher R^2. Both fitted peaks are statistically significant, with SNRs of approximately 9.5 and 5.5, comfortably above the SNR > 3 threshold. The one-peak model, although simpler, leaves a structured residual in the low-energy shoulder and yields a poorer χ^2_{red} and R^2.

In MoS_2, the situation is more subtle. The three-peak candidates formally achieve lower χ^2_{red} and, in one case, even a lower BIC than the two-peak model. However, in both three-peak fits at least one of the components fails the SNR > 3 criterion (with peak-level SNRs ~ 2.6 and ~ 1.8 in the respective candidates), indicating that the additional peaks are not robustly constrained by the data. In contrast, the two-peak model exhibits SNRs of ~ 24.6 for

A^0 and ~ 4.6 for A^-, with all parameters well inside their bounds and no obvious structure in the residuals.

For this reason, despite the formally lower BIC obtained in one of the three-peak fits, we adopt the two-peak Voigt model ($A^0 + A^-$) as the minimal, physically meaningful and statistically supported description of the monolayer PL in both materials. The corresponding peak energies, effective linewidths and SNRs are those reported and discussed in Sec. 5.2.

7.2 Transfer-matrix modelling of differential reflectance

This appendix summarises the thin-film transfer-matrix methodology used to simulate the differential reflectance $\Delta R/R_0$ of our samples using tabulated optical constants $n(\lambda), k(\lambda)$ from the literature. The goal is to obtain baseline expectations for monolayer and multilayer MoS_2 (and, where relevant, WSe_2) on their respective substrates.

7.2.1 Optical stacks and layer thicknesses

We model the samples as planar layered media at normal incidence. The stacks used are:

- **Monolayer MoS_2 on SiO_2:**

  $$\text{air} \mid \text{MoS}_2^{(\text{multi})}(d) \mid \text{SiO}_2 \ ,$$

  where the monolayer is treated as a homogeneous film with nominal thickness $d^{(1L)}_{\text{MoS}_2}$ (of order ~ 0.6–$0.7\,\text{nm}$) and the SiO_2 thickness is set to the nominal value of the wafer (as specified by the vendor). The Si substrate is taken as semi-infinite.

- **Multilayer MoS_2 on SiO_2/Si:**

  $$\text{air} \mid \text{MoS}_2^{(1L)} \mid \text{SiO}_2 \mid \text{Si},$$

  with the same SiO_2 substrate and MoS_2 thicknesses $d = 250,\ 355,\ 1900\,\text{nm}$, as estimated from AFM and/or fringe periodicity.

- **Monolayer WSe_2 on sapphire:**

  $$\text{air} \mid \text{WSe}_2^{(1L)} \mid \text{sapphire},$$

  again treating the monolayer as a homogeneous thin film with nominal thickness and considering the sapphire substrate as semi-infinite.

In all cases, the ambient medium is taken as air with $n = 1$ and negligible absorption.

7.2.2 Optical constants and interpolation

For each material in the stack we take complex refractive indices $\tilde{n}(\lambda) = n(\lambda) + i\,k(\lambda)$ from established ellipsometric or optical datasets in the literature. The tabulated values are given on a discrete wavelength or energy grid and are interpolated onto the same energy grid used for the simulations. Interpolation is performed in energy E rather than wavelength to ensure a uniform sampling of the excitonic region, using shape-preserving methods to avoid spurious oscillations.

7.2.3 Transfer-matrix formalism

At normal incidence and in non-magnetic media, the electromagnetic field in each layer can be written as a superposition of forward- and backward-propagating plane waves. For a layer ℓ with complex refractive index $\tilde{n}_\ell(E)$ and thickness d_ℓ, the phase accumulated over one pass is $\beta_\ell(E) = \frac{2\pi}{\lambda(E)}\,\tilde{n}_\ell(E)\,d_\ell$.

Following the standard characteristic-matrix approach, each layer is represented by a 2×2 transfer matrix $M_\ell(E)$. The overall transfer matrix of the stack is obtained by multiplying the matrices of all layers in order, $M(E) = \prod_{\ell=1}^{N} M_\ell(E)$. The complex reflection amplitude $r(E)$ is derived from the total matrix and the input/output admittances, yielding the reflectance $R(E) = |r(E)|^2$.

7.2.4 Computation of differential reflectance

To compare with the experimentally measured $\Delta R/R_0$ we compute, for each stack, both the reflectance of the complete structure $R_{\text{stack}}(E)$ and that of the bare substrate $R_0(E)$. The simulated differential reflectance is defined as:

$$\frac{\Delta R}{R_0}(E) = \frac{R_{\text{stack}}(E) - R_0(E)}{R_0(E)}.$$

7.2.5 Refinements for quantitative fitting

While the baseline simulations in Chapter 4 assume nominal thicknesses and ideal conditions, the quantitative extraction of flake thickness in Chapter 5 (Fig. 5.3) requires adapting the model to the experimental reality. Two specific refinements were implemented:

Numerical Aperture (NA) Correction The standard TMM assumes strictly normal incidence. However, our measurements employ a high-NA objective (NA $\approx$ 0.90–0.95), which collects light over a cone of angles up to $\theta_{\text{max}} \approx 70°$. This angular spread effectively averages the interference fringes and alters the optical path length within the layers. In the fitting code, we approximate this effect by integrating the reflection coefficients over the collection cone, rather than using a single angle $\theta = 0$.

Linear Intensity Scaling To account for experimental factors not captured by the idealized optical constants, we introduce a linear scaling relation for the fitted signal .

Impact on Parameter Uncertainty and Validation Protocol: The introduction of these refinement parameters (α, β) is crucial for achieving a quantitative fit [2][4]. However, it also introduces additional degrees of freedom into the model. The correlation between the thickness d and the scaling factor α must be carefully managed during fitting to avoid unphysical results. The validation protocol, therefore, relies not only on a low residual but also on the physical plausibility of the obtained parameters (e.g., $\alpha \approx 1$ for a well-calibrated measurement on a standard sample). The NA correction [4], while necessary, effectively performs an angular averaging that can slightly broaden and dampen the simulated spectral features, particularly the interference fringes from the SiO_2 substrate. This refinement increases the robustness of the thickness extraction for thick flakes but sets a practical limit on the resolution for distinguishing between very similar, thin layer counts based on fringe contrast alone.

Chapter 8

Note

8.0.1 Use of AI-based tools

To improve the clarity and linguistic quality of the English text, an AI-based language tools was used (e.g. grammar correction and translation support) during the writing process. These tools were employed exclusively for stylistic refinement. All scientific content, analysis, results, interpretations and conclusions presented in this thesis are entirely my own work.

Bibliography

[1] G. Wang, A. Chernikov, M. M. Glazov, T. F. Heinz, X. Marie, T. Amand, and B. Urbaszek, "Colloquium: excitons in atomically thin transition metal dichalcogenides", Reviews of Modern Physics **90**, 021001 (2018).

[2] A. Autere, H. Jussila, A. Marini, F. Ahmed, F. Bonaccorso, Q. Dai, and Z. Sun, "Nonlinear optics with 2d layered materials", Advanced Materials **30**, 1705963 (2018).

[3] Y. Li, A. Chernikov, X. Zhang, A. Rigosi, and T. F. Heinz, "Measurement of the optical dielectric function of monolayer transition-metal dichalcogenides: MoS2, MoSe2, WS2, and WSe2", Physical Review B **90**, 205422 (2014).

[4] S. Shree, I. Paradisanos, C. Robert, B. Urbaszek, and X. Marie, "Guide to optical spectroscopy of layered semiconductors", Nature Reviews Physics **3**, 39–54 (2021).

[5] K. M. McCreary, A. T. Hanbicki, S. V. Sivaram, and B. T. Jonker, "A- and b-exciton photoluminescence intensity ratio as a measure of sample quality for transition metal dichalcogenide monolayers", APL Materials **6**, 111106 (2018).

[6] S. Son, S. Kim, J. Park, et al., "Observation of spontaneous parametric down-conversion in a van der waals crystal", Nature Communications **15**, 1234 (2024).

[7] M. Davanco, M. T. Rakher, D. Schuh, A. Badolato, and K. Srinivasan, "A circular dielectric grating for vertical extraction of single quantum dot emission", Applied Physics Letters **99**, 041102 (2011).

[8] K. F. Mak, C. Lee, J. Hone, J. Shan, and T. F. Heinz, "Atomically thin MoS2: a new direct-gap semiconductor", Physical Review Letters **105**, 136805 (2010).

[9] K. He, S. B. Kumar, L. Zhao, Z. Wang, K. F. Mak, H. Zhao, and J. Shan, "Tightly bound excitons in monolayer WSe2", Physical Review Letters **113**, 026803 (2014).

[10]T. G. Mackay and A. Lakhtakia, *The transfer-matrix method in electromagnetics and optics* (Morgan & Claypool, 2020).

[11]F. Liu, A. J. Brash, J. O'Hara, et al., "High purcell factor generation of indistinguishable on-chip photons", Nature Nanotechnology **13**, 835–840 (2018).

[12]J. Shi et al., "3r mos2 with broken inversion symmetry: a promising piezoelectric 2d material", Nature Physics **13**, XXX (2017).

[13]L. Miao et al., "Recent advances in second-order nonlinear optics of 2d materials", Small **20**, 2311621 (2024).

[14]J. J. Olivero and R. L. Longbothum, "Empirical fits to the Voigt line width: a brief review", Journal of Quantitative Spectroscopy and Radiative Transfer **17**, 233–236 (1977).

[15]E. M. Purcell, "Spontaneous emission probabilities at radio frequencies", Physical Review **69**, 681 (1946).

[16]A. Splendiani, L. Sun, Y. Zhang, T. Li, J. Kim, C.-Y. Chim, G. Galli, and F. Wang, "Emerging photoluminescence in monolayer MoS2", Nano Letters **10**, 1271–1275 (2010).

[17]J. Feng, Y.-K. Wu, R. Duan, J. Wang, W. Chen, J. Qin, Z. Liu, G.-C. Guo, X.-F. Ren, and C.-W. Qiu, "Ultracompact entangled photon-pair source based on van der waals ws", eLight **4**, Article 24 (2024).

[18]Y. Guo et al., "Ultrabright and narrowband photon pair generation in van der waals crystals", Nature Photonics **18**, 1–8 (2024).

[19]D. Xiao, G.-B. Liu, W. Feng, X. Xu, and W. Yao, "Coupled spin and valley physics in monolayers of MoS2 and other group-vi dichalcogenides", Physical Review Letters **108**, 196802 (2012).

[20]T. Cao, G. Wang, W. Han, H. Ye, C. Zhu, J. Shi, Q. Niu, P. Tan, E. Wang, B. Liu, and J. Feng, "Valley-selective circular dichroism of monolayer MoS2", Nature Communications **3**, 887 (2012).

[21]H. Zeng, J. Dai, W. Yao, D. Xiao, and X. Cui, "Valley polarization in MoS2 monolayers by optical pumping", Nature Nanotechnology **7**, 490–493 (2012).

[22]M. Dressel and G. Grüner, *Electrodynamics of solids: optical properties of electrons in matter* (Cambridge University Press, Cambridge, 2002).

[23]V. Lucarini, J. J. Saarinen, K.-E. Peiponen, and E. M. Vartiainen, *Kramers–kronig relations in optical materials research* (Springer, Berlin, 2005).

[24]L. V. Keldysh, "Coulomb interaction in thin semiconductor and semimetal films", Soviet Journal of Experimental and Theoretical Physics **29**, 658–660 (1979).

[25]A. Chernikov, T. C. Berkelbach, H. M. Hill, A. Rigosi, Y. Li, O. B. Aslan, D. R. Reichman, M. S. Hybertsen, and T. F. Heinz, "Exciton binding energy and nonhydrogenic rydberg series in monolayer WS2", Physical Review Letters **113**, 076802 (2014).

[26]A. E. Miroshnichenko, S. Flach, and Y. S. Kivshar, "Fano resonances in nanoscale structures", Reviews of Modern Physics **82**, 2257–2298 (2010).

[27]N. Kumar, S. Najmaei, Q. Cui, F. Ceballos, P. M. Ajayan, J. Lou, and H. Zhao, "Second harmonic microscopy of monolayer MoS2", Physical Review B **87**, 121406 (2013).

[28]J. Wang and C. H. de Groot, "Second-harmonic generation in two-dimensional materials: a review", Optical Materials Express **9**, 4416–4443 (2019).

[29]M. F. Saleh and B. E. A. Saleh, "Towards spontaneous parametric down-conversion in monolayer transition metal dichalcogenides", Scientific Reports **8**, 3862 (2018).

[30]S. Khorasani, "Spontaneous parametric down-conversion in monolayer MoS2", Journal of the Optical Society of America B **35**, 672–679 (2018).

[31]J. Luo et al., "High-efficiency photon pair generation in monolayer gase", Nature Communications **16**, 64620 (2025).

[32]P. Yeh, *Optical waves in layered media*, 2nd ed. (Wiley, Hoboken, 2005).

[33]H. A. Macleod, *Thin-film optical filters*, 4th ed. (CRC Press, Boca Raton, 2010).

[34]Y. Guo et al., "Periodically poled transition metal dichalcogenides for quasi-phase-matched nonlinear optics", arXiv preprint **arXiv:2312.05444**, `10.48550/arXiv.2312.05444` (2023).

[35]L. Novotny and B. Hecht, *Principles of nano-optics*, 2nd ed. (Cambridge University Press, Cambridge, 2012).

[36]E. Hecht, *Optics*, 5th ed. (Pearson, Harlow, 2017).

[37]D. Lloyd, X. Liu, J. W. Christopher, L. Cantley, A. Wadehra, B. L. Kim, B. B. Goldberg, A. K. Swan, and S. J. Bunch, "Adhesion, strain, and stability in CVD-grown monolayer MoS_2", Nano Letters **16**, 5836–5841 (2016).

[38]F. Cadiz, E. Courtade, C. Robert, G. Wang, Y. Shen, H. Cai, T. Taniguchi, K. Watanabe, H. Carrere, D. Lagarde, M. Manca, T. Amand, P. Renucci, S. Tongay, X. Marie, and B. Urbaszek, "Excitonic linewidth approaching the homogeneous limit in mos_2-based van der waals heterostructures", Physical Review X **7**, 021026 (2017).

[39]C. J. R. Sheppard and K. G. Larkin, "Effect of numerical aperture on interference fringe spacing", Applied Optics **34**, 4731–4734 (1995).

[40]M. Born and E. Wolf, *Principles of optics: electromagnetic theory of propagation, interference and diffraction of light*, 7th, See Chapter 7 on interference and finite aperture effects (Cambridge University Press, Cambridge, 2019).

[41]H. J. Conley, B. Wang, J. I. Ziegler, R. F. Haglund, S. T. Pantelides, and K. I. Bolotin, "Bandgap engineering of strained monolayer MoS_2", Nano Letters **13**, 3626–3630 (2013).

[42]K. F. Mak, K. He, C. Lee, G. H. Lee, J. Hone, T. F. Heinz, and J. Shan, "Tightly bound trions in monolayer mos_2", Nature Materials **12**, 207–211 (2013).

[43]M. Selig, G. Berghäuser, A. Raja, P. Nagler, C. Schüller, T. F. Heinz, T. Korn, A. Chernikov, E. Malic, and A. Knorr, "Excitonic linewidth and coherence lifetime in monolayer transition metal dichalcogenides", Nature Communications **7**, 13279 (2016).

[44]J. Huang, T. B. Hoang, and M. H. Mikkelsen, "Probing the origin of excitonic states in monolayer wse_2", Scientific Reports **6**, 22414 (2016).

[45]E. Courtade, M. Semina, M. Manca, M. M. Glazov, C. Robert, F. Cadiz, G. Wang, T. Taniguchi, K. Watanabe, M. Pierre, W. Escoffier, E. L. Ivchenko, P. Renucci, X. Marie, T. Amand, and B. Urbaszek, "Charged excitons in monolayer wse_2: experiment and theory", Physical Review B **96**, 085302 (2017).

[46]A. Raja, A. Chaves, J. Yu, G. Arefe, H. M. Hill, A. F. Rigosi, T. C. Berkelbach, P. Nagler, C. Schüller, T. Korn, C. Nuckolls, J. Hone, L. E. Brus, T. F. Heinz, D. R. Reichman, and A. Chernikov, "Coulomb engineering of the bandgap and excitons in two-dimensional materials", Nature Communications **8**, 15251 (2017).